An Integrated Method for Reconstructing Daily MODIS Land Surface Temperature Data

Gang Yang, Weiwei Sun, *Member, IEEE*, Huanfeng Shen, *Senior Member, IEEE*, Xiangchao Meng, and Jialin Li

***Abstract*—Land surface temperature (LST) is a critical parameter in land surface process. The Moderate Resolution Imaging Spectroradiometer (MODIS) can be used to generate various LST data products, and these data have been widely applied in many studies. Unfortunately, cloud contamination brings about numerous missing or abnormal values, which negatively affect the application of LST data. To reconstruct missing values and improve data quality, this paper proposes an integrated method for reconstructing LST data under two conditions: Clear sky and cloudy sky. For the clear-sky condition, the MODIS eight-day LST (MOD11A2) product is used to be interpolated into the low-quality daily LST dataset using the harmonic analysis of time series (HANTS) algorithm. And then the linear regression algorithm is implemented on the original good-quality pixels of the MODIS daily LST (MOD11A1) product. After that, seamless processing on the reconstructed low-quality daily LST dataset is carried using the Poisson image editing method, and finally the high-quality daily LST dataset under clear-sky condition are then obtained. For the cloudy-sky conditions, the revised neighboring-pixel (NP) algorithm that originates from the surface energy balance theory is used to reconstruct the real LST data. To evaluate the reconstruction performance under clear-sky condition, a simulated dataset is generated from simulated missing pixels with good quality that are randomly chosen from 98 available LST images in the year 2010. Meanwhile, the real LST measurements collected from ground sites are used to assess the reconstructed results under cloudy-sky condition. Satisfactory validation results show that the proposed integrated method effectively reconstructs the missing information and low-quality pixels caused by cloud cover and other factors. The filled data can seamlessly preserve the temporal and spatial consistence of the daily LST data, which do promote the practical utility of the MODIS LST product.**

Manuscript received August 2, 2018; revised December 22, 2018; accepted January 23, 2019. Date of publication February 28, 2019; date of current version March 25, 2019. This work was supported in part by the Natural Science Foundation of Zhejiang province under Grant LQ18D010001, in part by the General Project of Zhejiang Education Department under Grant Y201635661, in part by the National Natural Science Foundation under Grants 41801256 and 41671342, in part by the NSFC-Zhejiang Joint Fund for the Integration of Industrialization and Informatization under Grant U1609203, and in part by the K. C. Wong Magna Fund in Ningbo University. *(Corresponding authors: Gang Yang and Huanfeng Shen.)*

G. Yang, W. Sun, and J. Li are with the Department of Geography and Spatial Information Techniques, Ningbo University, Ningbo 315211, China (e-mail: love64080@163.com; sunweiwei@nbu.edu.cn; lijialin@nbu.edu.cn).

H. Shen is with the School of Resource and Environmental Sciences and the Collaborative Innovation Center of Geospatial Technology, Wuhan University, Wuhan 430079, China (e-mail: shenhf@whu.edu.cn).

X. Meng is with the Faculty of Electrical Engineering and Computer Science, Ningbo University, Ningbo 315211, China (e-mail: mengxiangchao@nbu.edu.cn).

Color versions of one or more of the figures in this paper are available online at http://ieeexplore.ieee.org.

Digital Object Identifier 10.1109/JSTARS.2019.2896455

***Index Terms*—Harmonic analysis of time series (HANTS), land surface temperature (LST), Moderate Resolution Imaging Spectroradiometer (MODIS), reconstruction, surface energy balance.**

I. Introduction

LAND surface temperature (LST) playsan essential role in understanding the energy exchange between land and atmosphere, urban climatology, and global environment change [1]–[3]. LST observations are therefore widely used in various scientific fields, including climatology, hydrology, agriculture, ecology, environmental science, and military reconnaissance [4]–[8]. Due to the large spatial heterogeneity of land cover and the complexity of the spatiotemporal distribution of surface temperature, conventional ground stations cannot collect spatially consistent and temporally continuous measurements over a wide area. In contrast, satellite-based thermal remote sensing is the only effective technique available to provide LST observations at regional and global scales with acceptable temporal resolution and completely spatial coverage [9]–[11]. Since the urgent need for long-term remotely sensed LST data in globe warming studies, the retrieval of the LST from remotely sensed thermal infrared (TIR) data has attracted much attention from remote sensing researchers in recent decades. Several classical retrieval methods, such as the split-window algorithm, the monowindow algorithm, and the single-channel algorithm, have been widely used in LST retrieval for various satellite data [12]–[17]. The Moderate Resolution Imaging Spectroradiometer (MODIS) onboard the Terra (morning) and Aqua (afternoon) platforms can provide successive daily LST products on a global scale that are retrieved with the generalized split-window algorithm [18]. However, a key issue should be noted that all the algorithms mentioned above can only work well when the data are acquired under clear-sky condition without any instrument faults. Unfortunately, the cloudy-sky condition in reality takes more than half of the actual day-to-day weather around the globe [19]. The optical band signals from the land surface cannot penetrate clouds. If solar radiation were obstructed by cloud and/or impacted by other atmospheric disturbances, land surface spectral signals would be mixed with or totally blocked by the cloud. Half of the total pixels would be missing if cloudy areas in the image were excluded during further analysis. The incompleteness and uncertainties caused by cloud coverage seriously hinder subsequent performance of satellite-derived LST data in realistic applications.

On the purpose of improving the practical utilities of remotely sensed LST data, techniques are requiring to effectively fill data gaps and eliminate cloud interference. Satellite-derived LST measurements are unavailable under prolonged periods with overcast skies [20]. Few studies have focused on the reconstruction techniques in two different sky conditions, i.e., clear sky and cloudy sky. For the clear-sky condition, the spatial information and multitemporal observations are usually used to estimate the missing LST values. Typical examples of spatial information based methods are the inverse distance weighting, spline function, geostatistical interpolation method, and multivariable interpolation algorithm [20]–[23]. The spatial information based methods rely only on limited spatial information and climate factors that are difficult to obtain precisely. That usually leads to an unsatisfactory accuracy of the reconstructed LST data. In addition, [24] proposed a spectral-angle distance-weighting reconstruction method, in which the land surface was quantitatively considered by calculating spectral angles of original multispectral images, but the climate factors were not taken into account. Different from the spatial information based methods, the temporal information based methods use more information acquired from the data at other times. Crosson *et al.* [25] used LST from the Terra/MODIS (morning overpass) to fill missing LST data of the Aqua/MODIS (afternoon overpass). Xu and Shen [11] used the harmonic analysis of time series (HANTS) algorithm to reconstruct the MODIS eight-day LST via removing cloud-affected observations by pixel-by-pixel harmonic fitting in time domain. Unfortunately, extreme events may not be well characterized in the HANTS algorithm. After that, [26] developed a multitemporal classifier and a robust temporal regression algorithm to fill invalid LST values, which reconstructed LST values accurately, with much less reference data. Recently, [27] proposed a remotely sensed daily LST reconstruction (RSDAST) model to fill the gaps in the MODIS daily LST product. The model assumes that the LST difference between nearby pixels is small during a short time period. One of the common deficiencies of aforementioned reconstructed methods is that they deal with the problem of ideal clear-sky LST values rather than the real LST under cloudy-sky condition.

Actually, the clouds significantly affect the surface energy budget resulting that the cloud-covered LST is lower than that of cloud-free during daytime. The cloud effects then should be considered in the reconstruction process to reconstruct the LST data under cloudy-sky condition. Jin [19] proposed a "neighboring-pixel" (NP) approach on the basis of surface energy balance principle. The NP approach fills the LST of cloudy pixels by using the spatially and temporally neighboring clear pixels, and several factors, such as the net solar radiation, net longwave radiation, latent heat flux, and other drive variables should be precisely determined. After that, [9] estimated the LST of cloudy pixels by exploiting the temporal domain offered by the Spinning Enhanced Visible and Infrared Imager onboard the geostationary Meteosat Second Generation. Then, a spatial and temporal NP algorithm was proposed to reconstruct cloud-contaminated pixels in daily MODIS LST product [28]. Later, [29] combined MODIS and AMSR-E data with Bayesian maximum entropy method to reconstruct high-quality LST data. Recovering real LST data under cloud depends on a complicated physical relationship between clear and cloudy LST. Additional variables of these above-mentioned methods are mandatorily required to estimate regional parameters and build the physical relationship. That makes the above-mentioned methods difficult to implement in realistic applications. In response to the above-mentioned problems, [30] has developed a method for cloudy LST information reconstruction. However, this method is not suitable for the reconstruction of long time-series data and large area missing data.

The object of this study is to reconstruct the daily MODIS LST products by developing an integrated method, where the temporal domain information based strategy is used to estimate the missing LST pixels under clear-sky condition, and the revised NP method is used to fill the gaps of the LST pixels under cloudy-sky condition. Different from other study, we fully consider the LST reconstruction under two different sky conditions, the integrated method is more flexible in response to different application purposes. In particular, the revised NP method makes it easier to implement with fewer parameters.

The arrangement of the paper is as follows. Section II describes the dataset including satellite and ground-based measurements. Section III presents the methodology of the integrated method. Section IV shows experimental results from the integrated method and HANTS algorithm, and the qualitative and quantitative evaluation results are compared with the measurements recorded at ground level under different sky conditions. In the end of this section, some discussions will be made for the results. Section V draws conclusions of the paper.

II. Data

A. MODIS Data

The MODIS LST products are generated as a sequence of products beginning with a swath (scene) and progressing, through spatial and temporal transformations, to daily, eight day and monthly global gridded products with different spatial resolutions [31]. In this study, we selected Collection-5 MODIS Terra LST products (MOD11A1 and MOD11A2) at 1-km spatial resolution for the year 2010. MOD11A1, the daily LST product, is used to develop the proposed method and validate results. MOD11A2, the eight-day LST product, is used to interpolate the daily LST as the auxiliary data. Only daytime LST (about 10:30 A.M.) of the tile h10v05 was chosen as the experimental data. Also, the MODIS normalized difference vegetation index (NDVI) products were chosen as an auxiliary data to determine the location of similar pixels and to assist in calculating LST from surface measurements. In order to maintain spatial and temporal consistency with surface temperature data, we selected MOD13A2, the 16-day NDVI product, at 1-km spatial resolution for the year 2010 of the tile h10v05. All the datasets were downloaded from website of NASA's Earth Observing System Data and Information System (http://reverb.echo.nas.gov/reverb/). The MODIS Reprojection Tool (MRT) was used to read files in HDF-EOS format, perform geographic transformations, clip the test data products, and to write the output to file formats other than HDF-EOS. Finally,

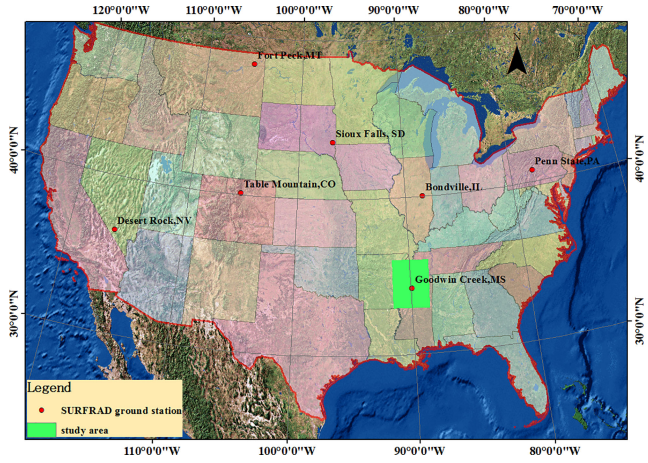

Fig. 1. Location of the study area and the distributions of the SURFRAD ground stations.

a subimage of 342 × 286 pixels located between 88.5 °E and 91.5 °E, and 33.0 °N and 36.0 °N was then extracted from all data products. As shown in Fig. 1, this area is located in midsouth of the United States, covering one Goodwin Creek (GWN) ground station of the Surface Radiation (SURFRAD) budget network. In addition, the Global Land Surface Satellite (GLASS) downwelling shortwave radiation product [32] provides shortwave radiation at 5-km resolution and was used in NP method. This dataset was downloaded from the website http://www.esrl.noaa.gov/gmd/grad/surfrad/.

Several preprocessing work was required for these MODIS data to ensure the successful operation of verification experiments. First, the cloud-contaminated pixels and other low-quality pixels were excluded with the help of the MODIS LST quality control (QC) flags, and the good-quality pixels recognized by QC flags were used to reconstruct contaminated pixels. Second, some good-quality pixels of the MOD11A1 products were masked randomly by different percentages as the simulated missing observations. All these simulated masked pixels would be reconstructed by our proposed method. The simulated missing observations are used to make a quantitative assessment. Third, we normalized LST, NDVI, and GLASS products through dividing all pixel values by 50, 10 000, and 100, respectively. Finally, the GLASS downward shortwave radiation product was resampled into 1-km spatial resolution.

B. Surface Measurements

The SURFRAD budget network was established in 1993 through the support of NOAA's Office of Global Programs, and its primary objective is to support climate research with accurate, continuous, long-term measurements pertaining to the SURFRAD budget over the United States (http://www.esrl.noaa.gov/gmd/grad/surfrad/overview.html) [33], [34]. The network has been used to provide the LST ground truth information for satellite-derived LST validation since the good continuity and high quality of the measurements [10].

TABLE I
DESCRIPTION OF MANDATORY QA FLAGS FOR THE MODIS LST PRODUCT [31]

Mandatory QA flags	Description
00	Pixel produced, good quality, not necessary to examine more detailed QA
01	Pixel produced, unreliable or unquantifiable quality, recommend examination of more detailed QA
10	Pixel not produced due to cloud effects
11	Pixel not produced primarily due to reasons other than cloud(such as ocean pixels, poor input data)

Fig. 1 shows that a total of seven SURFRAD sites are located in Montana, Colorado, Illinois, Mississippi, Pennsylvania, Nevada, and South Dakota. In this study, the ground-measurements from the Goodwin Creek (GWN) ground station were used to verify the performance of the reconstruction method. In order to keep the time consistent with the surface temperature data, we obtained the continuous upwelling and downwelling TIR radiation observations from this station in each morning of the year 2010 and used them to retrieve LST [35] with the following:

$$\mathrm{LST} = \left[F_{\mathrm{up}} - (1-\varepsilon)F_{\mathrm{dn}}\right] / (\varepsilon\sigma)^{1/4} \tag{1}$$

where F_{up} and F_{dn} are the upwelling and downwelling TIR radiation observations, respectively, and σ is the Stefan–Boltzmann constant. The broadband surface emissivity ε is estimated from the NDVI by employing the log linear relationship [36]

$$\varepsilon = 1.0094 + 0.047 \ln(\mathrm{NDVI}) \tag{2}$$

where NDVI is obtained from MOD13A2 product, and ln is the log operators. Equation (2) is obtained from regression analysis in NDVI values between 0.2 and 0.7, and it is not suitable for low NDVI values. The GWN ground station is located in the area of vegetation cover, and the NDVI has large values and could meet the requirement of (2).

C. Quality Analysis of the Test LST Data

The MODIS LST product provides QC information, and the QC can be used to determine the usefulness of the LST data for a user's needs [31]. The bit 1&0 of the QC scientific datasets (SDS), named as mandatory quality assurance (QA) flags, generally define the quality and application levels of each pixel (see Table I).

In this study, we analyzed the quality of the MODIS LST data for the study area. Fig. 2(a) shows the data quality of 365 MOD11A1 LST images in 2010. The percentages of high-quality LST values (QA = 00), low-quality LST values (QA = 01), missing LST values due to cloud coverage (QA = 10), and missing LST values due to other factors (QA = 11) are 32.06%, 9.35%, 55.59%, and 3%, respectively. Fig. 2 shows that many LST pixels are almost missing due to cloud coverage. Meanwhile, a single pixel appears to be continuous deletion in its long time series. The general spatial interpolation methods and time domain filtering methods cannot reconstruct the missing

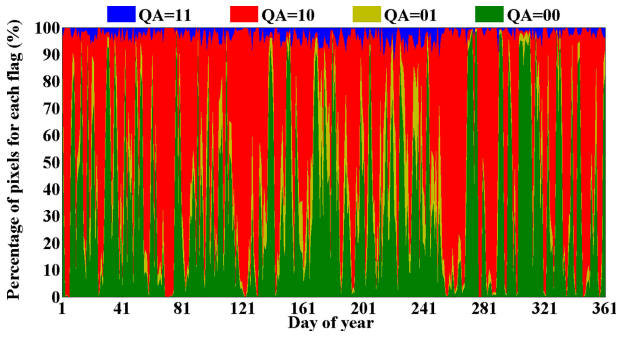

(a) Time variation of QA for MOD11A1 product

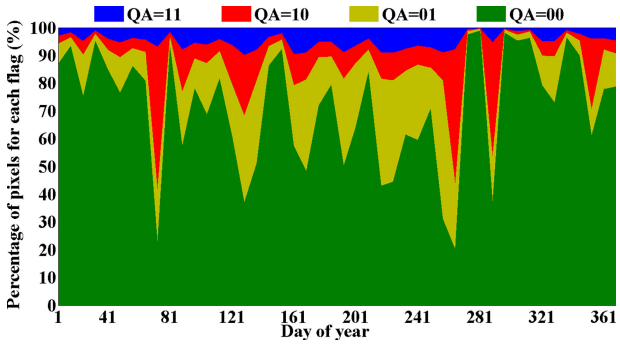

(b) Time variation of QA for MOD11A2 product

Fig. 2. Time variation of QA (refer to Table I) for the MODIS LST product. (a) Time variation of QA for MOD11A1 product. (b) Time variation of QA for MOD11A2 product.

information effectively. Therefore, it is of great significance to reconstruct the missing information by means of some auxiliary data.

Fig. 2(b) shows the data quality of 46 MOD11A2 LST images in 2010. The percentages of high-quality LST values (QA = 00), low-quality LST values (QA = 01), missing LST values due to cloud coverage (QA = 10), and missing LST values due to other factors (QA = 11) are 71.09%, 14.99%, 9%, and 4.92%, respectively. Compared with MOD11A1, the quality of MOD11A2 has been greatly improved. The explanation for that is the eight-day composite products improve the temporal and spatial integrity of the MODIS LST data to a certain degree. But the MOD11A2 still has missing information and low-quality information, and the adopted simple composite algorithms do not fully eliminate the cloud coverage. Fig. 2 shows that the missing pixels and the low-quality pixels have the smallest proportion in spring and winter, whereas they occupy the largest proportion in summer. The climate of study area is warm and humid, and particularly, its summer is wetter and lasts long. The proportions of both missing pixels and low-quality pixels of the synthetic data can reach up to more than 70%. Therefore, the quality of the composited LST data needs improving, and the temporal filter is usually an efficient strategy.

In addition, Fig. 3 shows the spatial distribution of missing information (QA = 10) percentage of the two sets of data at the pixel level over the whole year. For MOD11A1, more than half of the total pixels have more than 50% cloud coverage in one year, and only a small proportion of all pixels have less than 48% missing percentages through a year. For daily LST dataset,

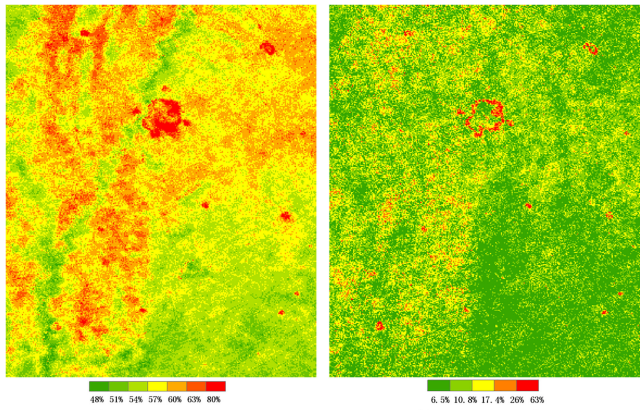

(a) MOD11A1 product (b) MOD11A2 product

Fig. 3. Spatial distribution of invalid data percentages in the MODIS LST data. (a) MOD11A1 product. (b) MOD11A2 product.

single pixel time series is prone to be continuous deletion in one year. In contrast, the missing proportions of most pixels in MOD11A2 product is less than 10.8%, and only a small proportion of missing pixels is greater than 17.4%. The quality of the composite LST data is much higher than that of the daily LST data, and therefore, we used eight-day composite LST product as auxiliary data for daily LST data reconstruction.

III. Methodology

Spatio-temporally complete daily MODIS LST data are generated by reconstructing the LST data in two conditions: 1) the clear-sky condition; and 2) the cloudy-sky condition. The first condition is to reconstruct low-quality LST pixels (QA = 01) and the missing LST pixels (QA = 11) due to other factors under clear-sky condition. In this condition, the missing LST pixels (QA = 10) due to cloud cover are also reconstructed, where the results are assumed under clear-sky condition. The second condition is to reconstruct the missing LST pixels (QA = 10) due to cloud cover spatially and temporally using the revised NP method. Fig. 4 shows the general process of the integrated method.

A. LST Reconstruction Under Clear-Sky Condition

MODIS daily LST products are with high cloud coverage in both spatial and temporal domain, and it results in a wide range of deletions in space and a continuous absence in time series. Using the auxiliary data is of great significance in reconstructing the daily LST products. LST is sensitive to the effects of surface roughness and vegetation, and is affected from land cover changes, and therefore we did not use the multiyear LST products as the auxiliary data. In order to satisfy the requirements of daily LST reconstruction, the MODIS eight-day LST products are selected. The right part of Fig. 4 shows the flow chart of its processing steps.

1) High-Quality Eight-Day LST Reconstruction: The eight-day LST still have pixel deletion and low-quality data. Therefore, it is necessary to promote the product quality before further applications. The HANTS algorithm [37], [38], developed based

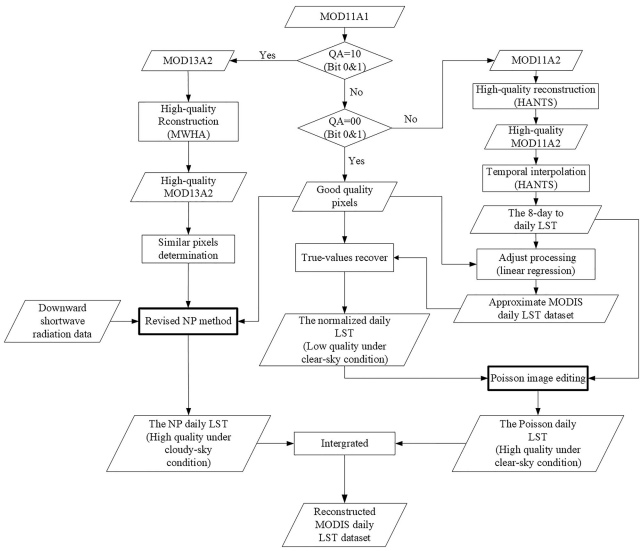

Fig. 4. General process of the integrated method.

on the Fourier transform, is an effective approach to reconstruct time series of remotely sensed products, such as NDVI, enhanced vegetation index (VI), and leaf area index [39]–[42]. It selects only the most significant frequencies in the time profiles and uses a least squares curve fitting procedure based on the harmonic components [43], shown as follows:

$$\widetilde{y} = a_0 + \sum_{k=1}^{nf} \left[a_k \cos(2\pi f_k t) + b_k \sin(2\pi f_k t)\right] \quad (3)$$

$$y(t) = \widetilde{y}(t) + \varepsilon(t), \quad t = 1, \ldots, N \quad (4)$$

where y, $\widetilde{y}$, and ε are the original time series, the reconstructed time series, and the error series, respectively. t is the time note of y, N is the length of the time series. a_k and b_k are the coefficients of the trigonometric components with the frequencies f_k, and nf is the number of harmonics associated with the frequencies f_k. It is an iterative process when implemented on time-series data, and the specific steps are described as follows [39].

1) Reject the pixels outside the valid range of data. For example, the valid range for LST can be 325–250, and the pixel values outside this range will be rejected.
2) Fit the remaining valid pixels by solving (3) using the least square method.
3) Repeat the algorithm until the maximum error between the current curve and the input data is smaller than a given threshold or the number of the remaining pixels is unnecessary for the reconstruction process.

Many studies have validated that LST varies periodically with season changes [44]–[46], and the HANTS algorithm has been proved to be successful in MODIS eight-day LST reconstruction [11]. So we implemented the HANTS algorithm in our study, and several parameters are carefully determined when applied to LST products. Table II shows that the SF was set at "low" because the presence of undetected clouds lowers the temperature of total pixels, thereby reducing surface temperature. By referring to other literature [11], the range of valid values is set within 250–325 K, and the FET is set as 6 K. The "NOF" is set as 3 through the parameter sensitivity analysis in Section IV.

TABLE II
PARAMETER SETTINGS OF HANTS IN THIS STUDY

Parameters	Description	Values
NOF	Number of frequencies	3
SF	The suppression flag indicating whether high or low values should be rejected during curve fitting	low
low	Low threshold	250
high	High threshold	325
FET	Fit error tolerance	6

Low-Quality Daily LST Reconstruction: This part is to reconstruct the low-quality daily LST dataset. As shown in Fig. 4, we first temporally interpolated the high-quality eight-day LST data into the coarse daily LST dataset by using the HANTS algorithm. The fitting result from the HANTS algorithm indicates the intra-annual variations of LST. We further obtained the interpolated daily LST data, and that properly indicates the periodic patterns of LST in time domain rather than the real LST. So some strategies are required to adjust the interpolated LST data into the real. In fact, the original MODIS daily LST products contain many good-quality pixels (QA = 00), and these pixels can be used to adjust the interpolated LST data. In this study, we adjusted the values of the interpolated LST data by establishing linear regression relationships between the good-quality pixels (QA = 00) of the original MODIS daily LST products and corresponding pixels of the interpolated daily LST data in pixel time series level. The original daily LST values were reconstructed where the pixels were flagged as good quality (QA = 00).

High-Quality Daily LST Reconstruction: After the last step, we obtained the normalized daily LST data. But some seams usually exist in the boundary between the good-quality areas and the reconstructed areas. We adopted the Poisson equation based interpolation machinery to seamlessly edit the image regions. The idea is the Poisson partial differential equation with Dirichlet boundary conditions, and it specifies the Laplacian of an unknown function over the domain of interest, along with the unknown function values over the domain boundary [47]. The Poisson equation can be solved by minimizing a L2-norm problem, and it computes the function whose gradient is the closest to some prescribed vector field under given boundary conditions. The basic equation is described as

$$\min_g \iint_B |\nabla g - \mathbf{v}|^2 \text{ with } g|_{\partial B} = g^*|_{\partial B} \quad (5)$$

where $\nabla . = [\frac{\partial .}{\partial x}, \frac{\partial .}{\partial y}]$ is the gradient operator. B is a closed subset of $A + B$ with boundary ∂B. g is an unknown scalar function defined over the interior of B. g^* is a known scalar function defined over A. v is guidance of vector field of a source closed subset C with function f.

The minimizer must satisfy the associated Euler–Lagrange equation and the unique solution follows Poisson equation with Dirichlet boundary conditions

$$\Delta g = \text{div } \mathbf{v} \text{ over } B, \text{ with } g|_{\partial B} = g^*|_{\partial B} \quad (6)$$

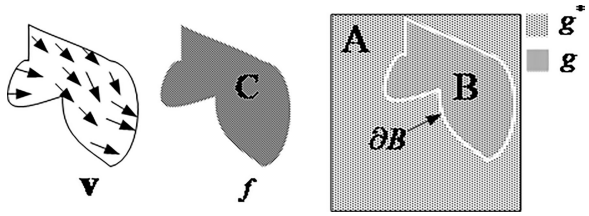

Fig. 5. Guided interpolation notations.

where $\Delta. = \frac{\partial^2 .}{\partial x^2} + \frac{\partial^2 .}{\partial y^2}$ is the Laplacian operator, and $\operatorname{div} v = \frac{\partial u}{\partial x} + \frac{\partial v}{\partial x}$ is the divergence of $v = (u, v)$.

The above-mentioned step is applied to all the reconstructed images because of the inevitable seams on the boundary between the reconstructed area and the original area. The boundary and seams can be identified according to QA flags. The QA $= 00$ and QA $\neq 00$ transition places are the boundary where the seam exists, and$B$ in Fig. 5 points to the reconstructed area obtained by linear regression. The pixel values of the area need to be corrected. v is the gradient field calculated based on guidance area C. This area does not need to have the true value, but it must have effective gradient information. The gradient information is obtained from the interpolated daily LST data from the HANTS algorithm. Although the reconstructed values of the intermediate product cannot represent the true value, it has the approximate correct gradient information. In conclusion, the guidance field of C is used to adjust the values of B via the Poisson equation with Dirichlet boundary conditions.

B. LST Reconstruction Under Cloudy-Sky Condition

The LST under clouds differ from that under clear-sky condition, due to the fact that clouds change the energy budget of the ground. In this study, we introduced the revised NP approach to reconstruct the LST under cloud [9], and the shortwave radiation data was chosen as the auxiliary data. The revised NP approach was developed on the basis of the theory of surface energy balance [19].

1) Revised NP Approach: Over the land surface, the relationship between energy fluxes is formulated as follows:

$$S_n - F_n = G + H + LE \tag{7}$$

where S_n is net solar (or shortwave) radiation deriving from incoming shortwave radiation minus outgoing shortwave radiation, and F_n is upwelling longwave radiation minus downwelling longwave radiation. G is the ground heat flux, and H and LE denote sensible heat flux and latent heat flux, respectively. For each item of (7), the partial derivative of T_s is obtained as follows:

$$\frac{\partial G}{\partial T_s} = \frac{\partial S_n}{\partial T_s} - \frac{\partial F_n}{\partial T_s} - \frac{\partial S_{hle}}{\partial T_s} \tag{8}$$

where S_{hle} is the sum of H and LE. $\partial S_n / \partial T_s$ does not mean net solar radiation, but is a function of T_s and it is only valid because S_n is equal to the Ts-related energy terms from (7). Using the conventional force-restore method [19], [48], [49], the ground heat flux is calculated by

$$G = k_g \frac{\partial T}{\Delta Z} = k_g \frac{T_s - T_d}{\Delta Z} \tag{9}$$

where k_g is the thermal conductivity of the ground soil in units $Wm^{-1}K^{-1}$, ΔZ is the penetration depth defined as a function of the thermal diffusivity which is the ratio of thermal conductivity to volumetric specific heat, and T_d is the temperature at the subsurface layer. The subsurface layer temperature T_d is much less sensitive than skin temperature to surface insolation [50], and the equation for two similar pixels can be written as

$$\frac{\partial G}{\partial T_s} = \frac{\partial}{\partial T_s}\left[k_g \frac{T_s - T_d}{\Delta Z}\right] \approx \frac{k_g}{\Delta Z}. \tag{10}$$

The linear relationships between F_n and S_n, and S_{hle} and S_n have been established by [19], which can be written as

$$F_n = a_0 + aS_n \tag{11}$$

$$S_{hle} = b_0 + bS_n \tag{12}$$

where a is a coefficient related to surface soil properties and b is a coefficient related to local surface and soil properties. Therefore, (11) and (12) can be written as follows:

$$\frac{\partial F_n}{\partial T_s} \approx \frac{\Delta F_n}{\Delta T_s} = \frac{\Delta F_n}{\Delta S_n}\frac{\Delta S_n}{\Delta T_s} = a \cdot \frac{\Delta S_n}{\Delta T_s} \tag{13}$$

$$\frac{\partial S_{hle}}{\partial T_s} \approx \frac{\Delta S_{hle}}{\Delta T_s} = \frac{\Delta S_{hle}}{\Delta S_n}\frac{\Delta S_n}{\Delta T_s} = b \cdot \frac{\Delta S_n}{\Delta T_s}. \tag{14}$$

Combining (10), (13), and (14), we can obtain (15) based on the assumption that the difference in net solar radiation as well as in surface temperature between two pixels or moments is only caused by clouds

$$\Delta T_s = \frac{\Delta Z}{k_g}(1 - a - b)\Delta S_n = \frac{1}{K}\Delta S_n \tag{15}$$

where $1/K = \Delta Z / k_g(1 - a - b)$, ΔT_s is the difference of LST between two similar pixels, and ΔS_n is the difference of net shortwave radiation between the two similar pixels.

Therefore, the LST under cloud can be written as

$$T_{\text{cloud}}(i) = T_{\text{clear}}(j) + \frac{1}{K}\Delta S_n(i, j) \tag{16}$$

where T_{cloud} is the LST pixel under cloud, T_{clear} is the spatially or temporally similar LST pixel under clear sky. K is the function of soil thermal conductivity, and ΔS_n is the difference of net shortwave radiation between the two similar pixels.

2) LST Reconstruction: Equation (16) indicates that the change of surface temperature not only has linear relation with the change of shortwave radiation, but also has direct relation with soil thermal conductivity. In this study, we assume that soil thermal conductivity will not change in a given range of regions and solve (16) by means of multiple regressions.

Accurate selection of similar pixels guarantees high precision reconstruction. Because of large amount of missing space in the surface temperature data, the target pixel value cannot be obtained, and the similar pixel extraction cannot be carried out using the LST data. The LST has a strong relation with the VI [51], [52]. Therefore, the MODIS 16-day NDVI data

(MOD13A2) is used as the assistant data for similar pixel extraction. A moving weighted harmonic analysis method [43] was utilized to improve the quality of the NDVI dataset. And an adaptive determination procedure for the similar pixel selection is then employed [53]. We choose the closest NDVI data to LST data in time as the reference data, and similar pixels are searched from common pixels using the following constraint:

$$|V_i - V_t| \le \Delta \tag{17}$$

$$\Delta = \sqrt{\sum_{i=1}^{n} (V_i - \mu)^2} \tag{18}$$

where V_t is the NDVI corresponding to the target LST, V_i is the *i*th similar NDVI, and Δ is the threshold value representing the local similarity related to the smoothness of adjacent areas, which is adaptively calculated by the local standard variation. μ is the mean value of all the NDVI in the local area (e.g., 5×5).

After determining the location of similar pixels by NDVI data, we remove the invalid positions in the three days before and after the date of a given cloudy pixel that were acquired using the QA information. An adaptive searching window centered on each contaminated pixel was used to select the similar pixels. If the desired number of similar pixels (e.g., 20) is not satisfied, the window size will be enlarged until the maximum size (e.g., 11×11).

IV. Results and Discussion

The integrated method generates spatio-temporally complete MODIS daily LST data. This is accomplished by analyzing one year of the MOD11A1 and MOD11A2 data from Terra on the test area as mentioned in Section II in order to illustrate the status of the test data. To evaluate the performance of the integrated method, we carried out the simulated and real experiments respectively. For the simulated experiments, we obtained simulated missing pixels where QA = 00 with different percentages for each of the images. The simulated missing pixels were reconstructed by the proposed method under clear-sky condition, and then they were compared with the original pixels. For the real experiments, the reconstructed pixels under two conditions were compared with the ground site measurements. The experimental results were quantitatively assessed using three statistical metrics. The following sections detail the qualitative and quantitative assessments for two conditions of the proposed method.

A. Evaluation Metrics

The first metric is the Pearson correlation coefficient (CC), which measures the degree of similarity between the reconstructed values and the original values as follows:

$$\mathrm{CC} = \frac{\sum_{j=1}^{M} (g_{\mathrm{re}(j)} - \overline{g_{\mathrm{re}}})(g_{\mathrm{or}(j)} - \overline{g_{\mathrm{or}}})}{\sqrt{\sum_{j=1}^{M} (g_{\mathrm{re}(j)} - \overline{g_{\mathrm{re}}})^2 (g_{\mathrm{or}(j)} - \overline{g_{\mathrm{or}}})^2}} \tag{19}$$

where $g_{\mathrm{re}(j)}$ and $g_{\mathrm{or}(j)}$ are the *j*th reconstructed and the original LST, respectively. $\overline{g_{\mathrm{re}}}$ and $\overline{g_{\mathrm{or}}}$ are their mean values, respectively, and M is the total number of contaminated pixels. The higher the metric value CC, the closer the two groups of values.

The second metric is the average absolute differences (AAD), which measures the amount of difference between the reconstructed data and the original data as follows:

$$\mathrm{AAD} = \frac{1}{M} \sum_{j=1}^{M} \left(\left| g_{\mathrm{or}(j)} - g_{\mathrm{re}(j)} \right| \right) \tag{20}$$

where M is the total number of contaminated pixels. $g_{\mathrm{re}(j)}$ and $g_{\mathrm{or}(j)}$ are the reconstructed and original values *j*th missing pixels, respectively.

The third metric is the root mean square error (RMSE). The metric is used to assess the deviation between reconstructed values and the original values. It is defined as

$$\mathrm{RMSE} = \sqrt{\sum_{j=1}^{M} (g_{\mathrm{re}(j)} - g_{\mathrm{or}(j)})^2 / (M-1)} \tag{21}$$

where M is the total number of contaminated pixels. $g_{\mathrm{re}(j)}$ and $g_{\mathrm{or}(j)}$ are the reconstructed and original values *j*th missing pixels, respectively. A smaller value indicates a closer similarity between the two groups of values.

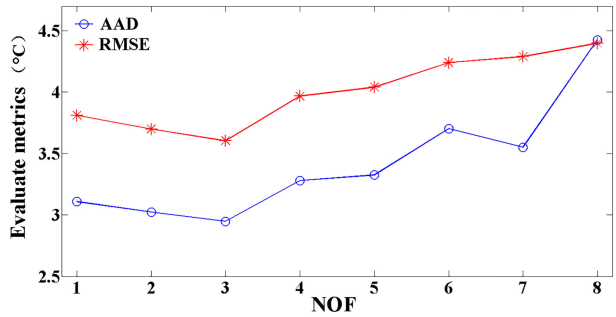

Fig. 6. Variations of RMSE and AAD with the NOF.

B. Parameter Sensitivity Analysis

The number of frequencies (NOF) is the main factor affecting the reconstruction accuracy. To determine the optimal setting for NOF, we carried out sensitivity analysis of the reconstruction accuracy to various NOF values.

For the composited LST products, the missing pixel values have no corresponding original LST observation data. Therefore, the missing pixels cannot be used to evaluate the reconstructed results. In order to evaluate the reconstruction results effectively, it is an effective method to evaluate the reconstructed results by selecting good-quality (QA = 00) pixels in surface temperature data as reference data. In this study, we selected two scene datasets on March 30, 2010 and October 12, 2010 to carry out the evaluation. We first make the simulated missing pixels with QA = 00 in different percentages on the two images. Then the simulated missing pixels were reconstructed by HANTS, so we obtained the reconstructed pixels and the original pixels. Fig. 6 shows the variations of RMSE and AAD with NOF varies from 1 to 8. The two quantitative metrics have similar tendency with the changing NOF. When the NOF is within 1–3, the two

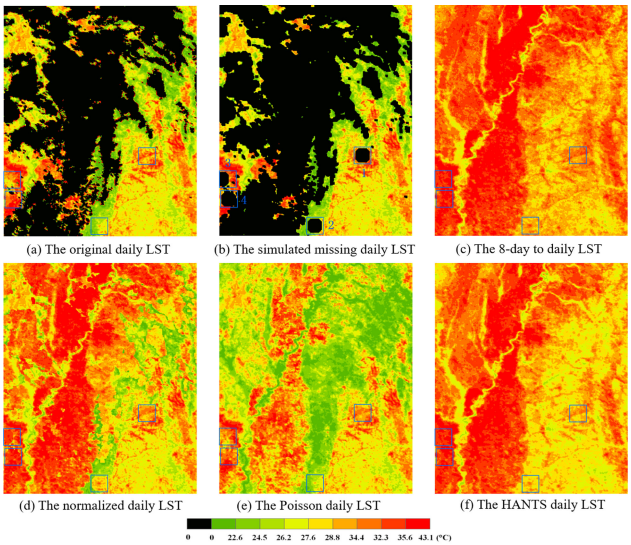

Fig. 7. Reconstruction daily LST on June 6, 2010 obtained from each step of the integrated method. The rectangles with solid line are the simulated missing area. (a) Original daily LST. (b) Simulated missing daily LST. (c) Eight-day to daily LST. (d) Normalized daily LST. (e) Poisson daily LST. (f) HANTS daily LST.

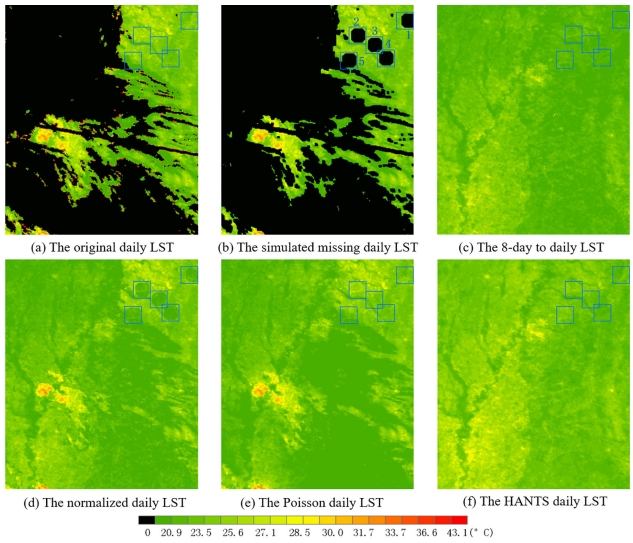

Fig. 8. Reconstruction daily LST on October 1, 2010 obtained from each step of the integrated method. The rectangles with solid line are the simulated missing area. (a) Original daily LST. (b) Simulated missing daily LST. (c) Eight-day to daily LST. (d) Normalized daily LST. (e) Poisson daily LST. (f) HANTS daily LST.

quantitative metrics show a decreasing trend. When the NOF is within 3–8, the two quantitative metrics show an increasing tendency. The two quantitative metrics reach the minimum when the NOF is 3. The smaller the two quantitative metrics, the smaller the deviation between the reconstructed data and the original data, and the higher the reconstruction accuracy. Thus, NOF was finally identified as 3 to reconstruct high-quality eight-day LST data.

C. LST Quality Assessment Under Clear-Sky Condition

In this part, we selected HANTS algorithm for comparison, because of its excellent performance in time-series data reconstruction. In order to evaluate the reconstructed results, we make the simulated missing pixels with QA = 00 randomly for the available data. Quality analysis results (in Section II) show that the amount of cloud cover varies among different days, and we selected 98 images with less than 65% cloud cover as the available data to evaluate the reconstructed results. After the reconstruction, the RMSE, AAD, and CC are calculated by comparing the reconstructed pixels with the original pixels of the simulated missing parts.

1) Qualitative Assessment: In order to demonstrate the gradual reconstruction process and to test the effectiveness of the LST reconstruction under clear-sky condition at a regional scale, we showed the examples of the original LST data, each step of the reconstruction LST data and the HANTS reconstructed LST data for the test area. With the consideration of the space limitations, we only listed the results of the LST data on June 6, 2010 and October 1, 2010 in Fig. 7 and Fig. 8, respectively. The results explain that this step of the integrated method reconstructs the visually spatial continuous LST data under clear-sky condition on the whole. Specifically, Figs. 7(a) and 8(a) show

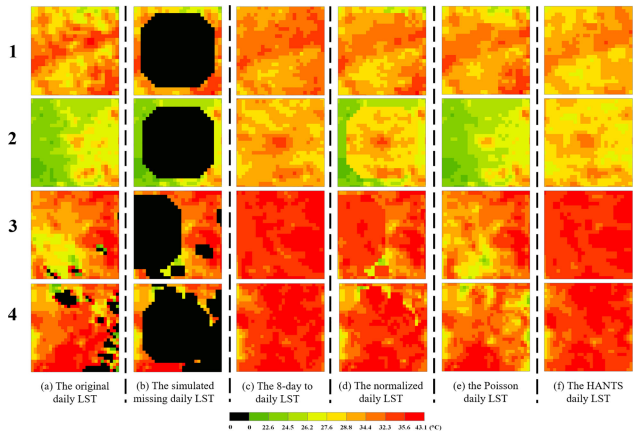

Fig. 9. Zoomed-in images of the simulated missing area 1–4 in Fig. 7, respectively.

the original daily LST data, where the cloudy pixels and the low-quality pixels are masked using the QA information. More than 50% missing information needs to be reconstructed. Figs. 7(b) and 8(b) show the simulated missing daily LST data, where some good-quality pixels have been masked randomly, shown as the places covered by blue rectangles. In this step, a number of points are generated randomly within the study area, and buffers with ten pixels as the radius are generated based on these points. The intersection of these buffers with high-quality pixels is the simulated missing part. Figs. 7(c) and 8(c) show the interpolated daily LST data from eight-day LST data by HANTS. Although the daily LST data can be interpolated by eight-day LST data, there is a serious inconsistency between the interpolation results and the original data, as the zoom-in images [1, 2, 3, 4 (a, c) in Fig. 9 and 1, 2, 3, 4, 5 (a, c) in Fig. 10] show that the LST

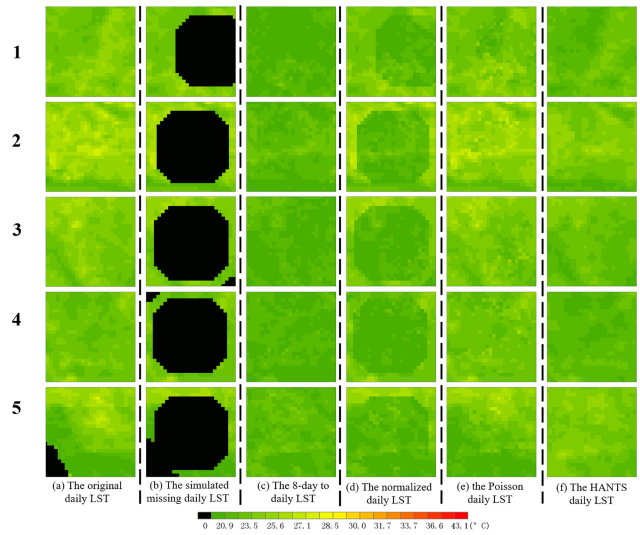

Fig. 10. Zoomed-in images of the first simulated missing area 1–5 in Fig. 8, respectively.

TABLE III
QUANTITATIVE EVALUATION OF THE TWO IMAGES

	June 6th, 2010			October 1st, 2010		
	CC	RMSE	AAD	CC	RMSE	AAD
8-day to daily LST	0.6873	3.6797	3.0564	0.4138	3.2043	2.9989
Normalized daily LST	0.7009	3.1300	2.5493	0.5002	3.0883	2.8509
Poisson daily LST	**0.9344**	**1.1247**	**0.8811**	**0.7983**	**0.9773**	**0.7709**
HANTS daily LST	0.61961	3.2640	2.6166	0.6324	1.6240	1.501

Bold entities indicate the optimal results.

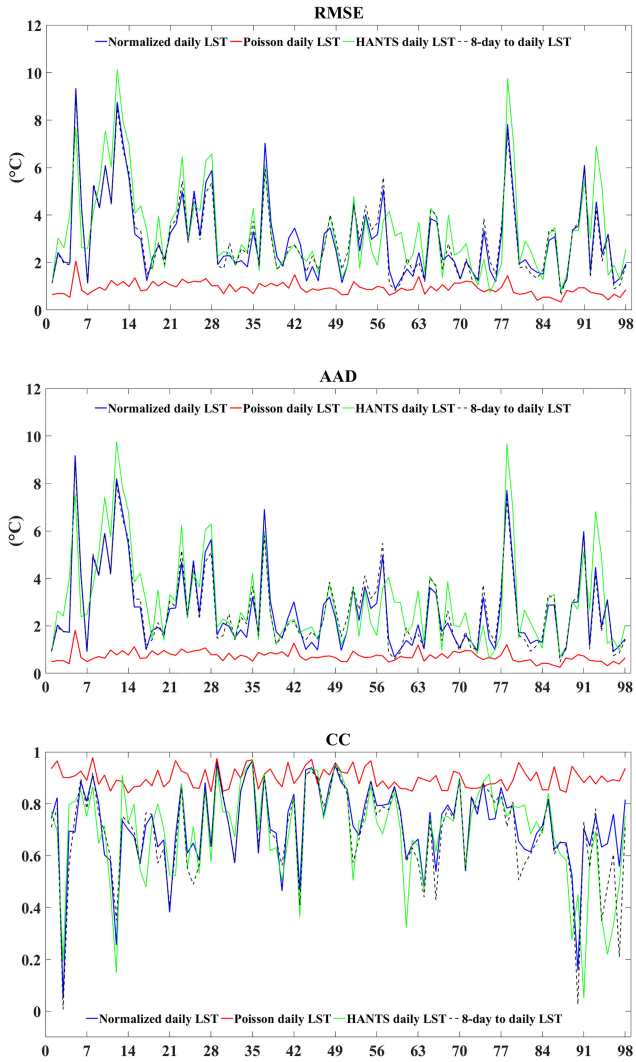

Fig. 11. Comparison curves of three evaluation metrics obtained from eight-day to daily LST, normalized daily LST, Poisson daily LST, and HANTS daily LST for the 98 selected images.

with same land cover type displays inconsistency between the interpolated results and the original data. Figs. 7(d) and 8(d) show the normalized daily LST data obtained by linear regression based on original LST values. Although all the gaps have been filled, some seams appear clearly at the boundary between good areas and the reconstructed areas, as the zoom-in images [1, 2, 3, 4 (d) in Fig. 9 and 1, 2, 3, 4, 5(d) in Fig. 10] show that the LST with same land cover type displays nonconsistent color appearance between the good areas and the reconstructed areas. Figs. 7(d) and 8(d) show the high-quality daily LST obtained after the Poisson image editing. All the seams are removed, and the land surface objects show normal LST [as zoomed in 1, 2, 3, 4 (e) in Fig. 9 and 1, 2, 3, 4, 5 (e) in Fig. 10], which are very close to the original LST [as zoomed-in images 1, 2, 3, 4 (a) in Fig. 9 and 1, 2, 3, 4, 5(a) in Fig. 10]. Figs. 7(f) and 8(f) show the reconstructed daily LST obtained from HANTS algorithm. The results illustrate that HANTS algorithm can generate spatio-temporal seamless LST data. However, the result value generally increases by comparing with the original data. Table III also shows that the Poisson daily LST has the optimal results. The LST data in Fig. 7 was selected on June 6 and is within the summer season, and hence the LST values show a clear grade division. In contrast, the LST data shown in Fig. 8 was selected in autumn season, and the LST values show a lower level. The LST results shown in Figs. 7 and 8 are consistent with their seasonal features. All the results show that this method can fill data gaps seamlessly and maintains the spatial and temporal integrity of the daily LST data.

2) Quantitative Assessment: In this paper, the quantitative assessment is implemented to evaluate the integrated method. For the quantitative assessment, we made simulated missing pixels with different percentages for each of the 98 available images. The simulated missing pixels were reconstructed by the proposed method and the HANTS algorithm. Then the quantitative assessment was given in three metrics by comparing the reconstructed values obtained from each step of the integrated method and the HANTS algorithm with the original values of the simulated missing areas.

We plotted the comparison curves of the three evaluation metrics for the 98 selected results obtained from each step of the integrated method and the HANTS algorithm in Fig. 11. And we

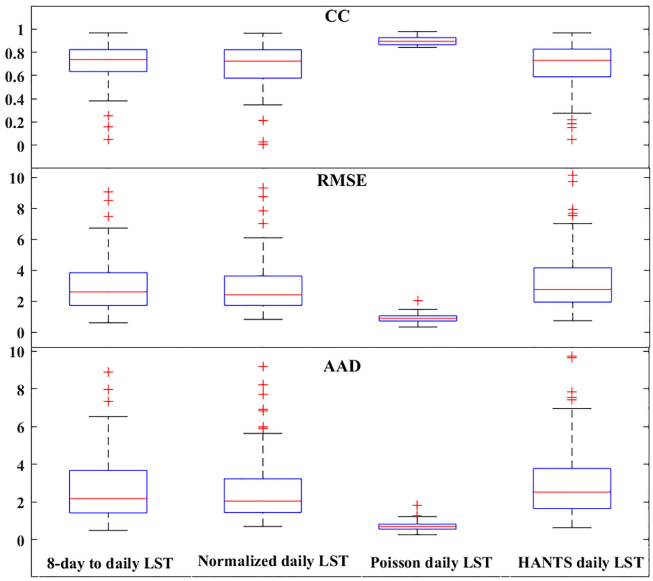

Fig. 12. Boxplot of three evaluation metrics obtained from eight-day to daily LST, normalized daily LST, Poisson daily LST and HANTS daily LST for the 98 selected images.

also carried on the statistical analysis using the three evaluation metrics for the 98 selected results obtained from each step of the integrated method and the HANTS algorithm in the form of boxplots in Fig. 12. The results of Poisson daily LST are much better than the other results, especially the results of HANTS daily LST. Specifically, RMSE and AAD preserve a high degree of consistency on the curve. The result curves before the Poisson image editing process fluctuate greatly, and it indicates that a large deviation exists between the reconstructed pixel values and the original pixel values. The result curves of HANTS algorithm perform worse. After Poisson image editing, the fluctuations of the curves are kept within a smaller numerical range, the upper limit of RMSE and AAD in Fig. 12 is less than 1.5 °C after the Poisson image editing process, and the median is kept within the range of 1 °C. The upper limit values of RMSE and AAD are close to 7 °C for the other results, especially the results of HANTS daily LST, and the distance between the upper four and the lower four points is large, indicating that the RMSE and AAD are highly variable. In Fig. 11, most CC values are less than 0.8 for the results before Poisson image editing and the HANTS daily LST. However, almost all of the CC values are greater than 0.85 for the results of Poisson daily LST. As can be seen from Fig. 12, the statistics of the 98 images CC values are in the vicinity of 0.8 before the Poisson image editing and the HANTS algorithm. However, the results of Poisson daily LST show that the upper and lower bounds and the upper and lower four points are within a very small range, indicating that the reconstruction results of all the selected images are of high accuracy.

In addition, the overall quantitative evaluation of all the missing pixels in the selected 98 images was also presented in this study. As shown in Table IV, the value of CC is increased from 0.9307 to 0.9926, and the RMSE and AAD are also improved by about 2 °C after the Poisson image editing. The HANTS

TABLE IV
OVERALL QUANTITATIVE EVALUATION OF THE MISSING PIXELS IN THE SELECTED 98 IMAGES

	CC	RMSE (℃)	AAD (℃)
8-day to daily LST	0.9287	3.3718	2.6687
Normalized daily LST	0.9307	3.3479	2.6102
Poisson daily LST	**0.9926**	**1.0832**	**0.7344**
HANTS daily LST	0.9048	3.8173	3.0508

Bold entities indicate the optimal results.

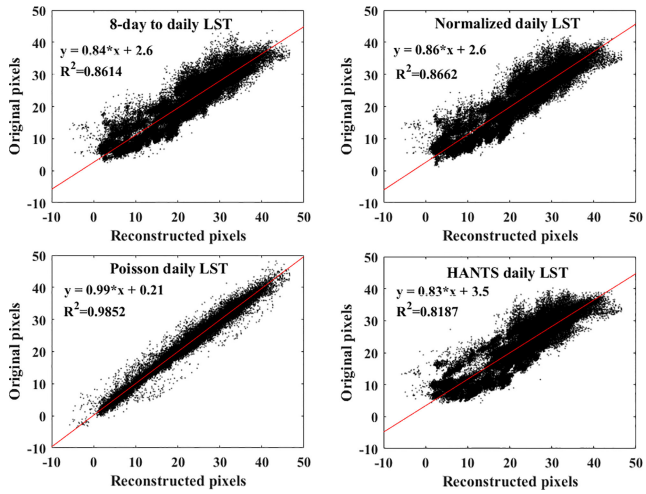

Fig. 13. Comparison of scatterplot of the reconstructed results of eight-day to daily LST, normalized daily LST, Poisson daily LST, and HANTS daily LST versus the original values for all the simulated missing pixels of the selected 98 images (note: $R = CC$).

daily LST has the worst performance for the three metrics. Fig. 13 shows the comparison of the scatterplot of the reconstructed results of eight-day to daily LST, normalized daily LST, Poisson daily LST, and HANTS daily LST versus the original values for all the simulated missing pixels of the selected 98 images. The pixel values of the Poisson daily LST are highly similar to the original pixel values, and these pixel values of the other daily LST are discrete to the original pixel values. All the verification results prove that the Poisson image editing method has played an important role in improving the accuracy of reconstruction results. And the part of the integrated method is superior to the HANTS algorithm in reconstructing LST under the clear-sky condition.

D. LST Quality Assessment Under Cloudy-Sky Condition

In order to better evaluate the accuracy of the reconstructed LST under cloud, we used the ground measurements as the real data to calculate the quantitative metrics. Also, quantitative and qualitative evaluations are still performed in this part.

1) Qualitative Assessment: In order to intuitively evaluate the reconstructed results under cloud, we carried out a comparison between the results under clear-sky condition and under cloudy-sky condition, as shown in Figs. 14 and 15. As a whole,

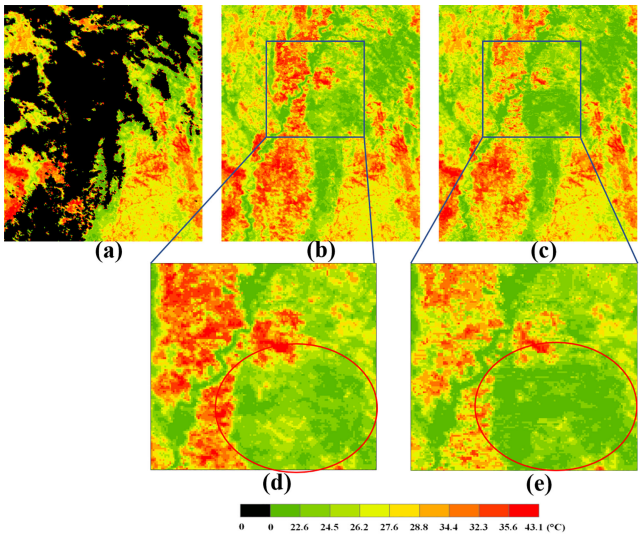

Fig. 14. Comparison of the reconstruction results under clear-sky conditions and under cloudy-sky conditions on June 6, 2010. (a) Original LST data. (b) Reconstructed result under clear-sky conditions. (c) Reconstructed result under cloudy-sky conditions. (d) Zoomed-in image of (b). (e) Zoomed-in image of (c).

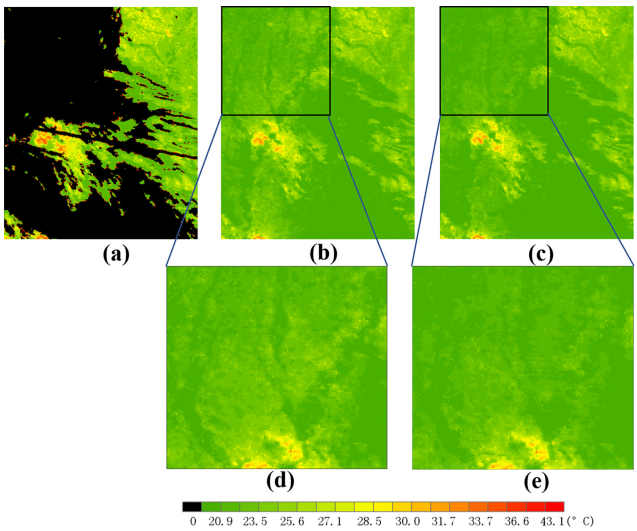

Fig. 15. Comparison of the reconstruction results under clear-sky conditions and under cloudy-sky conditions on October 1, 2010. (a) Original LST data. (b) Reconstructed result under clear-sky conditions. (c) Reconstructed result under cloudy-sky conditions. (d) Zoomed-in image of (b). (e) Zoomed-in image of (c).

the results under the cloud are different from those under clear-sky conditions, especially on June 6th, which is consistent with the previously described. The zoomed-in images illustrate that most of the reconstructed pixel values under the cloud are lower than those under clear-sky condition. But some pixel values are still higher than those in clear sky. Moreover, the reconstruction results after NP method are not maintaining spatial detail information, as shown in the red oval of the zoomed-in images. Some explanations have been described in discussion.

In addition, we also compared the reconstructed results to the ground measurements in time domain. The SURFRAD GWN site is located in this test area, from which we can obtain the

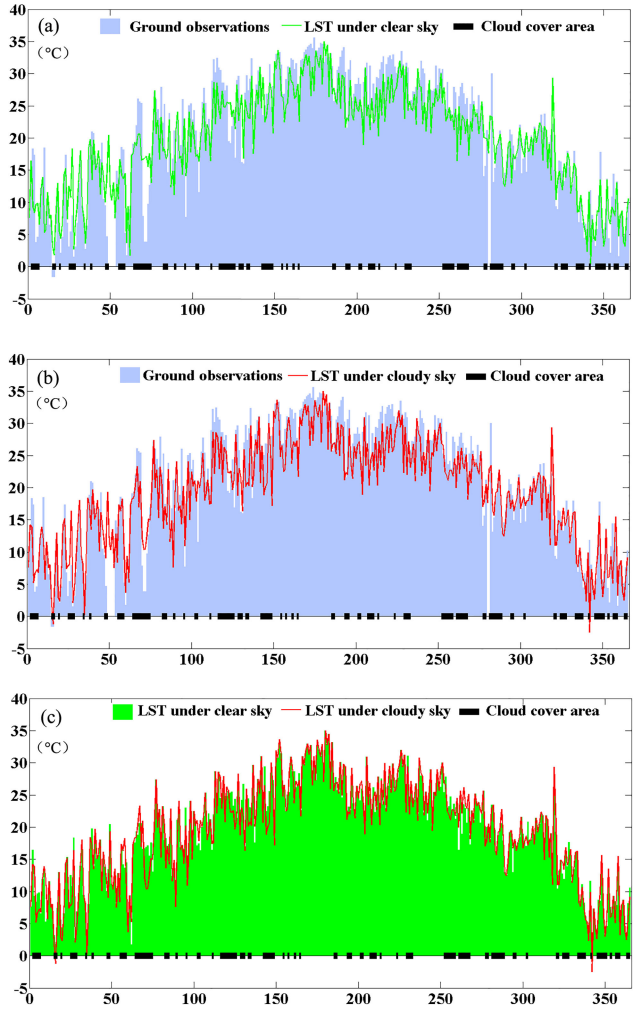

Fig. 16. Comparison of temporal variations between any two datasets. (a) Comparison between the ground observations and the reconstructed LST under clear-sky condition. (b) Comparison between the ground observations and the reconstructed LST under cloudy-sky condition. (c) Comparison between the reconstructed LST under clear-sky condition and that under cloudy-sky condition.

high-quality upwelling and downwelling TIR data to accurately retrieve the LST data. To keep in line with the MODIS Terra satellite transit time, we chose the retrieved LST data for each morning of the year 2010 as the ground truth to compare with the reconstructed data in the corresponding location. Fig. 16 shows the comparison of temporal variations between any two datasets. The reconstruction results under clear-sky condition differ slightly from those of reconstructed under cloud. However, the temporal variation trends of the two datasets remained highly consistent. The temporal variation trends of the two datasets are consistent with the ground measurements, although there are some differences compared with the measured data. More specifically, the reconstructed LST under cloud are closer to the ground measurements by visual inspection.

2) Quantitative Assessment: We further calculated RMSE, AAD, and CC to evaluate the reconstructed results under different sky conditions. There are nine invalid data and 356 valid data in the 365 ground observations, and 201 valid days are under

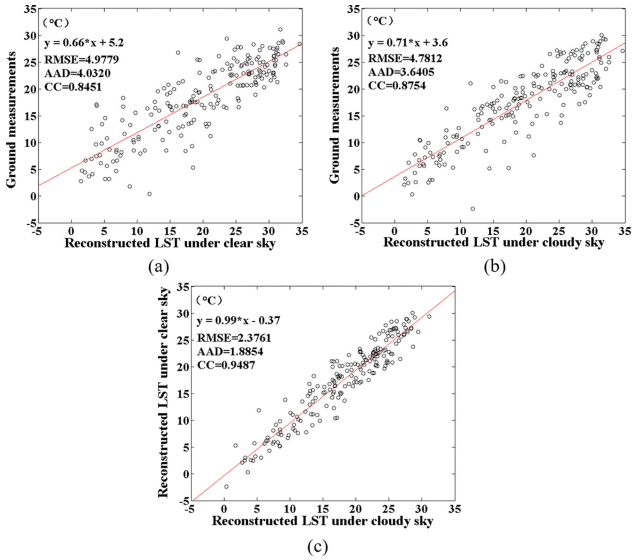

Fig. 17. Comparison of temporal variations between any two sets of data. (a) Comparison between the ground observations and the reconstructed LST under clear-sky condition. (b) Comparison between the ground observations and the reconstructed LST under cloudy-sky condition. (c) Comparison between the reconstructed LST under clear-sky condition and those under cloudy-sky condition.

cloud cover. Three metrics are calculated based on the 356 valid data. Fig. 17(a) shows that the CC between the reconstructed LST under clear-sky conditions and the ground measurements is 0.8451, and RMSE and AAD are 4.9779 and 4.0320 °C, respectively. Fig. 17(b) shows that after the revised NP method, the CC, RMSE, and AAD between ground measurements and the reconstructed LST are 0.8754, 4.7812 and 3.6405 °C, respectively. Although the differences of the three metrics are very small, it shows that the reconstructed LST after the revised NP method are closer to the ground measurements. In other words, shortwave downwelling radiation data play a key role in reconstructing the LST under cloud. We also compared the reconstructed LST under clear-sky condition and those under cloudy-sky condition. The three metrics (CC, RMSE, and AAD) are 0.9487, 2.3761, and 1.5488 °C, respectively. These three quantitative evaluation results indicate that there is a high correlation between the reconstructed LST under different sky conditions, and the clouds can do to reduce the LST by about 2 °C. Overall, the reconstructed LST after the revised NP method are prior to those under the clear-sky condition.

E. Discussion

The simulated experiments indicated that the proposed method effectively reconstructs LST under clear-sky condition. All the LST of the reconstructed pixels were highly consistent with that of the original pixels. The real experiments also illustrated that the reconstructed MODIS LST values are quite approaching the ground measurements. Therefore, the proposed method can reconstruct MODIS LST accurately under different sky conditions. However, some factors that affect the accuracy of the results need to be discussed.

1) Necessity of the Eight-Day LST Product: The daily LST data not only contain a large amount of missing information in space, but also show a continuous absence in time. The classical gap-filling methods are difficult to effectively reconstruct the missing information of these data due to unavailable reference data. Also, the temporal filter methods cannot fit the right curves to reflect the real change trend in a continuous absence. Therefore, the auxiliary data are needed to provide effective reference data as much as possible. In this study, the eight-day LST products were used due to their higher quality after the composite method and some temporal filter methods were proven to be effective in reconstructing high-quality remotely sensed composited products. The eight-day LST product fits the complete temporal variation information of LST after the high-quality reconstruction, which could be used in the daily LST product reconstruction.

2) Cloud Effects: The QA flag records the quality of each pixel in the LST products, indicating the available pixels and the cloud-cover pixels. The locations of clouds were determined by the MODIS cloud mask algorithm using a series of visible and infrared threshold. However, effects of cloud edges, such as cloud shadows, have a very substantial impact on satellite land products. They degrade the quality of clear-sky composite products and bring about systematic biases in long-term data records [27], [54]. Although we have masked all the pixels except these pixels with good quality (QA = 00), it might fail to mask the edge of the clouds, as the images in Figs. 7(a) and 8(a) show that many red and trivial patches appear on the edge of valid data regions. Apparently, this effect would bring about errors to our reconstructed results. Therefore, we carried out corrosion algorithm to clear these red and trivial patches, as the images denoted in Figs. 7(b) and 8(b) show, in order to minimize the influence of the cloud edge.

3) Downwelling Shortwave Radiation Product Effect: In this study, the revised NP method was used to reconstruct the LST under cloudy-sky condition. The NP method regarded that the change of surface temperature not only has linear relation with the changing shortwave radiation, but also has direct relation with soil thermal conductivity. Actually, soil thermal conductivity is affected by many other parameters and is difficult to obtain. Therefore, an assumption was made that soil thermal conductivity did not change in a given range of regions, and the downwelling shortwave radiation data were chosen as the only auxiliary data. This assumption may lead to a lot of errors to the reconstructed results, as shown in the red oval of the zoomed-in images in Figs. 14 and 15. In addition, the downwelling shortwave radiation data in this paper were calculated by complementary calculation of the data of various sensors, and we confirmed by the producer that there were indeed some of the outliers in the data and they were difficult to be identified. Although many methods have been developed for removing noises, it is difficult to eliminate these outliers correctly in this paper. So some errors have been introduced leading to some of the reconstructed pixel values under the cloudy-sky condition higher than those under clear-sky condition.

V. Conclusion

MODIS LST products are negatively affected by cloud and cloud shadows resulting in many invalid or missing LST values. An analysis of the MODIS LST product in 2010 for the test area indicated that the percentage of high-quality LST values in the daily LST product for this region was only 32.06%, whereas the percentage of low-quality LST values was 9.35%, and the percentage of missing LST values due to cloud coverage was 55.59%. MODIS daily LST data are heavily affected by cloud cover, and it is of great significance to reconstruct the missing information caused by cloud cover. Although the eight-day composite LST products are with higher quality, the integrity of this data needs to be improved before their further applications.

In this study, an integrated method has been developed to reconstruct the MODIS daily LST product, which consists of two parts. First, the LST reconstruction under clear-sky condition, where the MODIS eight-day LST product was used to be interpolated into the low-quality daily LST dataset using the HANTS method before the linear regression based on the original good quality pixels of the MODIS daily LST product. And then the Poisson image editing method was used for seamless processing of the reconstructed low-quality daily LST dataset to generate high-quality daily LST dataset under clear-sky condition. Second, the LST reconstruction under cloudy-sky condition, where the revised NP approach based on the theory of surface energy balance was used to reconstruct the real LST under cloud with the help of the downwelling shortwave radiation data.

The reconstructed LST under clear-sky condition was evaluated using the simulated experiments by masking the good quality pixels and then reconstructing valid LST pixels. We have calculated the CC, RMSE, and AAD for each of the selected 98 images as well as the overall simulated missing pixels between reconstructed pixel values and the original pixel values. The reconstructed LST shows the overall accuracy with CC of 0.9926, and RMSE of 1.0832 °C, and AAD of 0.7344 °C. All the results show that the Poisson image editing method plays an important role in improving the accuracy of reconstruction results. We have evaluated the reconstruction results under different sky conditions by comparing the reconstructed results to the ground measurements. The evaluated results (CC, RMSE, and AAD) under clear-sky condition are 0.8451 are 4.9779 and 4.0320 °C, as well as those under cloudy-sky condition are 0.9487, 2.3761°C, and 1.5488°C, respectively. The comparison between the results under clear-sky and cloudy-sky conditions indicate that there is a high correlation between the reconstructed LST under different sky conditions, and the clouds can do to reduce the LST by about 2 °C. In conclusion, the proposed method can reconstruct high-quality MODIS daily LST data products.

Acknowledgment

The authors would like to thank the editor and referees for their suggestions that improve this paper.

References

[1] Q. Weng and P. Fu, "Modeling annual parameters of clear-sky land surface temperature variations and evaluating the impact of cloud cover using time series of Landsat TIR data," *Remote Sens. Environ.*, vol. 140, no. 5, pp. 267–278, 2014.

[2] P. J. Sellers, F. G. Hall, G. Asrar, D. E. Strebel, and R. E. Murphy, "The first ISLSCP field experiment (FIFE)," *Bull. Amer. Meteorol. Soc.*, vol. 69, no. 1, pp. 22–27, 1987.

[3] J. A. Sobrino, J. E. Kharraz, and Z.-L. Li, "Surface temperature and water vapour retrieval from MODIS data," *Int. J. Remote Sens.*, vol. 24, no. 24, pp. 5161–5182, 2003.

[4] M. C. Anderson, J. M. Norman, W. P. Kustas, R. Houborg, P. J. Starks, and N. Agam, "A thermal-based remote sensing technique for routine mapping of land-surface carbon, water and energy fluxes from field to regional scales," *Remote Sens. Environ.*, vol. 112, no. 12, pp. 4227–4241, 2008.

[5] A. J. Arnfield, "Two decades of urban climate research: A review of turbulence, exchanges of energy and water, and the urban heat island," *Int. J. Climatol.*, vol. 23, no. 1, pp. 1–26, 2003.

[6] J. Hansen, R. Ruedy, M. Sato, and K. Lo, "Global surface temperature change," *Rev. Geophys.*, vol. 48, no. 4, p. RG4004, 2010.

[7] H. Shen, L. Huang, L. Zhang, P. Wu, and C. Zeng, "Long-term and fine-scale satellite monitoring of the urban heat island effect by the fusion of multi-temporal and multi-sensor remote sensed data: A 26-year case study of the city of Wuhan in China," *Remote Sens. Environ.*, vol. 172, pp. 109–125, 2016.

[8] M. G. Estes Jr. *et al.*, "Use of remotely sensed data to evaluate the relationship between living environment and blood pressure," *Environ. Health Perspect.*, vol. 117, no. 12, p. 1832, 2009.

[9] L. Lu, V. Venus, A. Skidmore, T. Wang, and G. Luo, "Estimating land-surface temperature under clouds using MSG/SEVIRI observations," *Int. J. Appl. Earth Observ. Geoinf.*, vol. 13, no. 2, pp. 265–276, 2011.

[10] S. Li, Y. Yu, D. Sun, T. Dan, X. Zhan, and C. Long, "Evaluation of 10 year AQUA/MODIS land surface temperature with SURFRAD observations," *Int. J. Remote Sens.*, vol. 35, no. 3, pp. 830–856, 2014.

[11] Y. Xu and Y. Shen, "Reconstruction of the land surface temperature time series using harmonic analysis," *Comput. Geosci.*, vol. 61, no. 4, pp. 126–132, 2013.

[12] J. C. Price, "Land surface temperature measurements from the split window channels of the NOAA 7 advanced very high resolution radiometer," *J. Geophys. Res. Atmos.*, vol. 89, no. D5, pp. 7231–7237, 1984.

[13] F. Becker and Z. Li, "Towards a local split window method over land surfaces," *Int. J. Remote Sens.*, vol. 11, no. 3, pp. 369–393, 1990.

[14] G. B. Franc and A. P. Cracknell, "Retrieval of land and sea surface temperature using NOAA-11 AVHRR data in north-eastern Brazil," *Int. J. Remote Sens.*, vol. 15, no. 8, pp. 1695–1712, 1994.

[15] Z. Wan and Z. L. Li, "A physics-based algorithm for retrieving land-surface emissivity and temperature from EOS/MODIS data," *IEEE Trans. Geosci. Remote Sens.*, vol. 35, no. 4, pp. 980–996, Jul. 1997.

[16] J. C. Jiménez-Muñoz and J. A. Sobrino, "A generalized single channel method for retrieving land surface temperature from remote sensing data," *J. Geophys. Res. Atmos.*, vol. 108, no. D22, pp. 2015–2023, 2003.

[17] Z. Qin, A. Karnieli, and P. Berliner, "A mono-window algorithm for retrieving land surface temperature from Landsat TM data and its application to the Israel-Egypt border region," *Int. J. Remote Sens.*, vol. 22, no. 18, pp. 3719–3746, 2001.

[18] Z. Wan and J. Dozier, "A generalized split-window algorithm for retrieving land-surface temperature from space," *IEEE Trans. Geosci. Remote Sens.*, vol. 34, no. 4, pp. 892–905, Jul. 1996.

[19] M. Jin, "Interpolation of surface radiative temperature measured from polar orbiting satellites to a diurnal cycle: 2. Cloudy pixel treatment," *J. Geophys. Res. Atmos.*, vol. 105, no. D3, pp. 4061–4076, 2000.

[20] S. Westermann, M. Langer, and J. Boike, "Spatial and temporal variations of summer surface temperatures of high-arctic tundra on Svalbard—Implications for MODIS LST based permafrost monitoring," *Remote Sens. Environ.*, vol. 115, no. 3, pp. 908–922, 2011.

[21] D. Cai, N. Guo, and L. I. Chongwei, "Interpolation of air temperature based on DEM over eastern region of Gansu," *J. Arid. Meteorol.*, 2009.

[22] M. Neteler, "Estimating daily land surface temperatures in mountainous environments by reconstructed MODIS LST data," *Remote Sens.*, vol. 2, no. 1, pp. 333–351, 2010.

[23] M. Metz, D. Rocchini, and M. Neteler, "Surface temperatures at the continental scale: Tracking changes with remote sensing at unprecedented detail," *Remote Sens.*, vol. 6, no. 5, pp. 3822–3840, 2014.

[24] T. Shuai *et al.*, "A spectral angle distance-weighting reconstruction method for filled pixels of the MODIS land surface temperature product," *IEEE Geosci. Remote Sens. Lett.*, vol. 11, no. 9, pp. 1514–1518, Sep. 2014.
[25] W. L. Crosson, M. Z. Al-Hamdan, S. N. J. Hemmings, and G. M. Wade, "A daily merged MODIS Aqua–Terra land surface temperature data set for the conterminous United States," *Remote Sens. Environ.*, vol. 119, no. 8, pp. 315–324, 2012.
[26] C. Zeng, H. Shen, M. Zhong, L. Zhang, and P. Wu, "Reconstructing MODIS LST based on multitemporal classification and robust regression," *IEEE Geosci. Remote Sens. Lett.*, vol. 12, no. 3, pp. 512–516, Mar. 2015.
[27] L. Sun *et al.*, "Reconstructing daily clear-sky land surface temperature for cloudy regions from MODIS data," *Comput. Geosci.*, vol. 105, pp. 10–20, 2017.
[28] W. Yu, M. Ma, X. Wang, and J. Tan, "Estimating the land-surface temperature of pixels covered by clouds in MODIS products," *J. Appl. Remote Sens.*, vol. 8, no. 14, p. 083525, 2014.
[29] X. Kou, L. Jiang, Y. Bo, S. Yan, and L. Chai, "Estimation of land surface temperature through blending MODIS and AMSR-E Data with the Bayesian maximum entropy method," *Remote Sens.*, vol. 8, no. 2, p. 105, 2016.
[30] C. Zeng, D. Long, H. Shen, P. Wu, Y. Cui, and Y. Hong, "A two-step framework for reconstructing remotely sensed land surface temperatures contaminated by cloud," *ISPRS J. Photogramm. Remote Sens.*, vol. 141, pp. 30–45, 2018.
[31] Z. Wan, "MODIS land surface temperature products users' guide," 2006. [Online]. Available: https://icess.eri.ucsb.edu/modis/LstUsrGuide/MODIS_LST_products_Users_guide_C5.pdf
[32] S. Liang *et al.*, "A long-term Global Land Surface Satellite (GLASS) data-set for environmental studies," *Int. J. Dig. Earth*, vol. 6, pp. 5–33, 2013.
[33] K. C. Wang and S. L. Liang, "Evaluation of ASTER and MODIS land surface temperature and emissivity products using long-term surface longwave radiation observations at SURFRAD sites," *Remote Sens. Environ.*, vol. 113, no. 7, pp. 1556–1565, 2009.
[34] J. A. Augustine, J. J. Deluisi, and C. N. Long, "SURFRAD-A national surface radiation budget network for atmospheric research," *Bull. Amer. Meteorol. Soc.*, vol. 81, no. 10, pp. 2341–2357, 2000.
[35] A. K. Inamdar, A. French, S. Hook, G. Vaughan, and W. Luckett, "Land surface temperature retrieval at high spatial and temporal resolutions over the southwestern United States," *J. Geophys. Res. Atmos.*, vol. 113, no. D7, pp. 1829–1836, 2008.
[36] A. A. V. D. Griend and M. Owe, "On the relationship between thermal emissivity and the normalized difference vegetation index for natural surfaces," *Int. J. Remote Sens.*,vol. 14, no. 6, pp. 1119–1131, 1993.
[37] M. Menenti, S. Azzali, W. Verhoef, and R. Van Swol, "Mapping agroecological zones and time lag in vegetation growth by means of Fourier analysis of time series of NDVI images," *Adv. Space Res.*, vol. 13, no. 5, pp. 233–237, 1993.
[38] W. Verhoef, "Application of harmonic analysis of NDVI time series (HANTS)," *Fourier Anal. Temporal NDVI Southern Afr. Amer. Continents*, vol. 108, pp. 19–24, 1996.
[39] G. J. Roerink, M. Menenti, and W. Verhoef, "Reconstructing cloudfree NDVI composites using Fourier analysis of time series," *Int. J. Remote Sens.*, vol. 21, no. 9, pp. 1911–1917, 2000.
[40] T. Westra and R. R. D. Wulf, "Monitoring Sahelian floodplains using Fourier analysis of MODIS time-series data and artificial neural networks," *Int. J. Remote Sens.*, vol. 28, pp. 1595–1610, 2007.
[41] X. Zhang, R. Sun, B. Zhang, and Q. Tong, "Land cover classification of the North China plain using MODIS_EVI time series," *ISPRS J. Photogramm. Remote Sens.*, vol. 63, no. 4, pp. 476–484, 2008.
[42] Y. Julien and J. A. Sobrino, "Comparison of cloud-reconstruction methods for time series of composite NDVI data," *Remote Sens. Environ.*, vol. 114, no. 3, pp. 618–625, 2010.
[43] G. Yang, H. Shen, L. Zhang, Z. He, and X. Li, "A moving weighted harmonic analysis method for reconstructing high-quality SPOT VEGETATION NDVI time-series data," *IEEE Trans. Geosci. Remote Sens.*, vol. 53, no. 11, pp. 6008–6021, 2015.
[44] Y. Julien, J. A. Sobrino, and W. Verhoef, "Changes in land surface temperatures and NDVI values over Europe between 1982 and 1999," *Remote Sens. Environ.*, vol. 103, no. 1, pp. 43–55, 2006.
[45] J. P. W. Scharlemann *et al.*, "Global data for ecology and epidemiology: A novel algorithm for temporal Fourier processing MODIS data," *PLoS One*, vol. 3, no. 1, pp. 1–13, 2008.
[46] V. D. Kerchove, L. Goossens, S. Lhermitte, and S. Veraverbeke, "Spatiotemporal variability in remotely sensed land surface temperature,;and its relationship with physiographic variables in the Russian Altay; mountains," *Int. J. Appl. Earth Obs. Geoinf.*, vol. 20, no. 2, pp. 4–19, 2013.
[47] P. Pérez, M. Gangnet, and A. Blake, "Poisson image editing," *Acm Siggraph*, vol. 22, no. 22, pp. 313–318, 2003.
[48] J. W. Deardorff, "Efficient prediction of ground surface temperature and moisture, with inclusion of a layer of vegetation," *J. Geophys. Res. Oceans*, vol. 83, no. C4, pp. 1889–1904, 1978.
[49] R. E. Dickinson, "The force-restore model for surface temperatures and its generalizations," *J. Climate*, vol. 1, no. 11, pp. 1086–1098, 1988.
[50] R. B. Stull, "An introduction to boundary layer meteorology," *Atmos. Sci. Library*, vol. 8 no. 8, p. 89, 1988.
[51] M. L. Jin and R. E. Dickinson, "Land surface skin temperature climatology: Benefitting from the strengths of satellite observations," *Environ. Res. Lett.*, vol. 5, no. 4, p. 044004, 2015.
[52] P. A. Schultz and M. S. Halpert, "Global analysis of the relationships among a vegetation index, precipitation and land surface temperature," *Int. J. Remote Sens.*, vol. 16, no. 15, pp. 2755–2777, 1995.
[53] C. Zeng, H. Shen, and L. Zhang, "Recovering missing pixels for Landsat ETM + SLC-off imagery using multi-temporal regression analysis and a regularization method," *Remote Sens. Environ.*, vol. 131, pp. 182–194, 2013.
[54] K. V. Khlopenkov and A. P. Trishchenko, "SPARC: New cloud, snow, and cloud shadow detection scheme for historical 1-km AVHHR data over Canada," *J. Atmos. Ocean. Technol.*, vol. 24, p. 322, 2007.

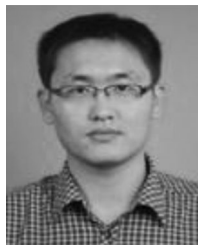

Gang Yang received the M.S. degree in geographical information system from the Hunan University of Science and Technology, Xiangtan, China, in 2012, and the Ph.D. degree in cartography and geographic information engineering from the School of Resource and Environmental Sciences, Wuhan University, Wuhan, China, in 2016. He is currently an Assistant Professor with Ningbo University, Ningbo, China.

His research interests include missing information reconstruction of remote sensing image, cloud removal of remote sensing image, and remote sensing time series products temporal reconstruction.

Weiwei Sun (M'15) received the B.S. degree in surveying and mapping, and the Ph.D. degree in cartography and geographic information engineering from Tongji University, Shanghai, China, in 2007 and 2013, respectively.

From 2011 to 2012, he was a Visiting Scholar with the Department of Applied Mathematics, University of Maryland, College Park, MD, USA, working with the famous Prof. J. Benedetto, studying the dimensionality reduction of hyperspectral image. From 2014 to 2016, he was a Postdoc with the State Key Laboratory for Information Engineering in Surveying, Mapping and Remote Sensing (LIESMARS), Wuhan University, Wuhan, China, where he studied intelligent processing in hyperspectral imagery. He is currently an Associate Professor with Ningbo University, Ningbo, China, and is also working as a Visiting Scholar with the Department of Electrical and Computer Engineering, Mississippi State University, MS, USA. He has authored more than 50 journal papers. His research interests include hyperspectral image processing with manifold learning, anomaly detection, and target recognition of remote sensing imagery using compressive sensing.

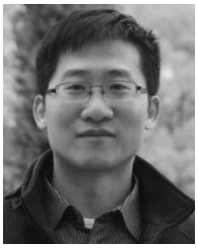

Huanfeng Shen (M'10–SM'13) received the B.S. degree in surveying and mapping engineering and the Ph.D. degree in photogrammetry and remote sensing from Wuhan University, Wuhan, China, in 2002 and 2007, respectively.

In July 2007, he joined the School of Resource and Environmental Sciences, Wuhan University, where he is currently a Luojia Distinguished Professor. He has authored more than 100 research papers. His research interests include image quality improvement, remote sensing mapping and application, data fusion and assimilation, and regional and global environmental change.

Dr. Shen has been supported by several talent programs, such as The Youth Talent Support Program of China (2015), China National Science Fund for Excellent Young Scholars (2014), the New Century Excellent Talents by the Ministry of Education of China (2011). He is currently a member of the Editorial Board of *Journal of Applied Remote Sensing*.

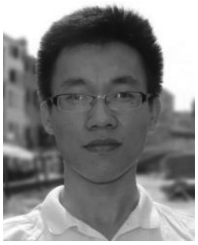

Xiangchao Meng received the B.S. degree in geographic information system from the Shandong University of Science and Technology, Qingdao, China, in 2012, and the Ph.D. degree in cartography and geography information system from Wuhan University, Wuhan, China, in 2017.

He is currently a Lecturer with the Faculty of Electrical Engineering and Computer Science, Ningbo University, Ningbo, China. His research interests include remote sensing image fusion and quality evaluation.

Jialin Li received the M.S. and the Ph.D. degrees in physical geography from Nanjing Normal University, Nanjing, China, in 1999 and 2004, respectively.

In 2012, he was a Visiting Scholar with Prof. Ruiliang Pu, with the School of Geosciences, University of South Florida, Tampa, USA, where he studied remote sensing application. He is currently a Professor with Ningbo University, Ningbo, China. His research interests include coastal remote sensing and coastal environmental evolution.